Vibrational Modes and Crystallographic Structure of Cd_3As_2 and $(Cd_{1-x}Zn_x)_3As_2$ Epilayers

B. Fluegel, A. D. Rice and K. Alberi

National Renewable Energy Laboratory, 15013 Denver West Parkway, Golden CO, 80401

Abstract

Low-temperature Raman scattering is used to study the crystal structure of molecular-beam epitaxially grown layers of the Dirac semimetal Cd_3As_2 and its related alloy $(Cd_{1-x}Zn_x)_3As_2$. The combination of narrow-linewidth spectra, multiple growth directions and full polarization analysis allows improved accuracy in identifying the irreducible representation of over 57 Raman-active vibrations. Several disagreements with previous identifications are found. Structurally, the results agree with the centrosymmetric $I4_1/acd$ space group of bulk-grown Cd_3As_2 and are clearly distinct from the Raman spectra of nanoscale platelets and wires. 3-fold twinning is seen in (112) Cd_3As_2 grown on (111) zincblende substrates corresponding to the three possible tetragonal orientations. In dilute $(Cd_{1-x}Zn_x)_3As_2$, phonons have a frequency and scattering amplitude dependence on Zn concentration that is continuous with Cd_3As_2 but at least one frequency is absent at the alloy endpoint, preventing a simple one-mode description of the alloy phonon.

1. Introduction

Cd_3As_2 is the most experimentally studied three-dimensional Dirac semimetal (DSM), a system in which a tetragonal distortion, vanishing bandgap and conical bands combine to form topologically protected bulk and surface electronic states [1]. These properties are intrinsically linked with the crystal structure. The rapid advances in the field have relied heavily on band structure computation and in turn on knowledge of its crystal structure, determined by Xray diffraction (XRD) [2] and electron diffraction [3] to be $I4_1/acd$. The centrosymmetry of bulk-grown Cd_3As_2, a strict requirement for a DSM, was resolved only recently [2], overturning 50-year old previous results [4] of a non-centrosymmetric group with similar XRD signal. Structure information specific to epitaxial thin films and the role of impurity atoms are also important. In Cd_3As_2 nanowires and nanobelts, a completely different crystal phase was observed using XRD and micro-Raman [5,6]. Similarly, Raman scattering of the related material Zn_3As_2 indicated different structures in molecular-beam epitaxy (MBE)- grown films [7] or nanoplatelets [8] compared to bulk crystals. In both materials it was reasoned that the templating influence of a substate [7] or the dominance of nanostructure surfaces [8] can alter the bulk crystal structure or cause a high-temperature phase to become room-temperature meta-stable. This phase was also stabilized in bulk crystals by alloying the two compounds [9]. These discrepancies are very important for Cd_3As_2 studies where alloying with Zn is calculated and experimentally employed to control doping and induce a transition from a DSM to trivial semiconductor [10]. With bulk-grown Cd_3As_2 and Zn_3As_2 belonging to different tetragonal space groups, the structure and Raman spectrum of the alloy are even less understood. This uncertainly in crystal structure arising from composition and synthesis methods can complicate studies where such knowledge is important, e.g., measuring quantized surface states, understanding the properties of bulk states, and designing the topological phase [11].

Raman scattering is thus a useful technique to aid XRD in uncovering the structure of Cd_3As_2 epitaxial layers and nanostructures and has the advantage of being particularly sensitive to centrosymmetry. Previous studies on vapor-phase grown bulk crystals have either used

incomplete polarization dependence [12], or have yielded spectra incompatible [13] with epitxial Cd_3As_2. Here we use polarized Raman scattering and selection rules for the particular backscattering directions that are accessible in MBE-grown films. These are the (112) direction, which allows all Raman-active modes, and the (001) direction, with a much-simplified spectrum. From this approach we identify the vibrational mode of each Raman frequency and compare with previous results from bulk-grown crystals, revealing notable differences. Rapid changes to the spectrum are seen with incorporation of small (< 5 at.%) concentrations of Zn, suggesting two-mode phonons or an abrupt change in the alloy crystal structure. Our results can be used as a guide to interpret results from alloys and epitaxial materials, where additional effects such as twinning may modify the Raman spectrum.

α-Cd_3As_2 was originally identified [4] from XRD as a body-centered tetragonal space group $I4_1cd$ with As atoms slightly distorted from a nominal zinc-blende sublattice. The 160-atom conventional cell that was presented in Ref. [4] has, per primitive cell, six sets of Cd atoms and three sets of As atoms, each of multiplicity 8 at C_1 sites, and two sets of As atoms (multiplicity 4) at sites that are of C_2 symmetry oriented along the tetragonal axis. The application of the correct factor group analysis [14] to the incorrect site symmetries noted in Ref. [13], resulted in an incorrect determination of the Raman active vibrational modes as $\Gamma^R = 26\ A_1 + 27\ B_1 + 27\ B_2 + 65\ E$ [13]. This spectrum was also claimed [15] for the α phase of Zn_3As_2 since it was found to have the same $I4_1cd$ structure [16,17]. The correct Raman modes for a compound of this space group and using the above site symmetries were given by Ref. [7] discussing bulk Zn_3As_2 and are $\Gamma^R = 28\ A_1 + 29\ B_1 + 29\ B_2 + 61\ E$.

Recently the Cd_3As_2 crystal structure has been reinvestigated [2] revealing that an alternate origin choice allows for a better fit of the XRD data to a centrosymmetric structure, $I4_1/acd$, also with 80 atoms per primitive cell. With the site symmetries given in that reference, the Raman modes are $\Gamma^R = 14\ A_{1g} + 14\ B_{1g} + 15\ B_{2g} + 31\ E_g$, the total being considerably reduced from the above cases because only the even vibrational modes are Raman-active.

Experimentally, these competing predictions can be compared with the number of observed Raman frequencies, which can only be a lower bound due to limitations of detection sensitivity

and resolution. Measurements to date have observed fewer lines than predicted and thus a centrosymmetric structure yields better agreement. In the case of Zn_3As_2, relatively few lines were resolved in early bulk-grown crystals (Ref. [15]). With improved spectra and polarization selection, a study of epitaxial Zn_3As_2 found at least 21 Raman lines [7]. This number still being far fewer than the $I4_1cd$ prediction, the authors concluded that their growth conditions had resulted in a new centrosymmetric phase with the unit cell halved. Similarly, early vapor-grown Cd_3As_2 showed only a few Raman lines [13] whereas a recent measurement [12] found that even with 44 observed lines, this still favored the more symmetric $I4_1/acd$ identification over $I4_1cd$. They compared only the total mode number and did not consider the correct analysis of the site symmetries of Ref. [4].

2. Method

Samples were grown as previously described [18] using MBE from elemental sources in a multi-chamber III-V, II-VI system with $Zn_{1-x}Cd_xTe$ buffer layers on GaAs substrates. The buffer layer results in lattice-matched growth, as seen in XRD [18]. Substrates were either on-axis (001) or (111) miscut 2° or 3° toward a $\langle\bar{1}\bar{1}2\rangle$ direction taken without loss of generality to be $[\bar{1}\bar{1}2]$. Some samples were grown using identical Cd_3As_2 conditions but with an added Zn flux, measured by a beam flux monitor. For Raman scattering, samples were oriented for backscattering with laser and analyzer polarizations aligned for a Cd_3As_2 c-axis that is parallel to the substrate's (001) axis. Previous works [19,20,18] have shown that (111) GaAs substrates miscut in the above manner will inhibit 180° twinning in (112) Cd_3As_2. Our results show that this can additionally inhibit 120° twinning yielding a single crystal structure; exceptions are discussed below. A continuous wave dye laser was spectrally filtered, linearly polarized, and focused to a 150 μm x 2000 μm line with an incident power of 20 mW. Scattered light was collected with an f/2 camera lens, analyzed through a rotating waveplate, and detected with a 640-mm subtractive triple Raman spectrometer and cooled CCD array having a spectral resolution of 1 cm^{-1}. Acquisition times were 3000 s. Frequencies from 15 cm^{-1} to 425 cm^{-1} were checked for comparison with other works. Laser excitation wavelengths through the red

spectral region as well as 515 nm were explored, showing a broad weak resonance near 645 nm similar to the results of Ref. [12]. All measurements shown here were at 645 nm and 4 K.

Successfully matching measured lines to an irreducible representation via the selection rules requires experimental access to specific crystal directions. Particularly useful is light propagation along the tetragonal axis using the four polarization combinations of Ref. [7]. Many modes can be eliminated in these cases, whereas light propagation normal to lower symmetry planes such as (112) in Ref. [12] only allows a partial intensity reduction. Here Raman was measured in the backscattering configuration parallel to each of the two growth directions, nominally $[001]$ and $\boldsymbol{g} \equiv [221]$. Plane and vector indices are given here in the tetragonal lattice $n_1 a\hat{\boldsymbol{x}} + n_2 a\hat{\boldsymbol{y}} + n_3 c\hat{\boldsymbol{z}}$ where approximately $a \approx c/2$. For growth along the tetragonal *c*-axis we employ laser and analyzer polarization directions $\boldsymbol{X} \equiv \hat{\boldsymbol{x}}$, $\boldsymbol{Y} \equiv \hat{\boldsymbol{y}}$, $\acute{\boldsymbol{X}} \equiv \frac{1}{\sqrt{2}}(\hat{\boldsymbol{x}} + \hat{\boldsymbol{y}})$, and $\acute{\boldsymbol{Y}} \equiv \frac{1}{\sqrt{2}}(\hat{\boldsymbol{x}} - \hat{\boldsymbol{y}})$. For growth on a cubic (111)-oriented substrate, the resulting Cd_3As_2 growth plane is (112) and we define within this plane unit vectors $\boldsymbol{C} \equiv \frac{1}{\sqrt{6}}(-\hat{\boldsymbol{x}} - \hat{\boldsymbol{y}} + 2\hat{\boldsymbol{z}})$ and $\boldsymbol{A} \equiv \acute{\boldsymbol{Y}}$ which are respectively the *c*-axis projection and its normal.

Table I shows the form of the Raman tensor for the two tetragonal crystal point groups that include proposed structures for room temperature α-Cd_3As_2 and Zn_3As_2. The degenerate modes are important here and we therefore write their contributions explicitly as in Ref. [21] where the scattering efficiency is proportional to

A_{1g}	B_{1g}	B_{2g}	E_g	E_g
$\begin{bmatrix} a & \cdot & \cdot \\ \cdot & a & \cdot \\ \cdot & \cdot & b \end{bmatrix}$	$\begin{bmatrix} c & \cdot & \cdot \\ \cdot & -c & \cdot \\ \cdot & \cdot & \cdot \end{bmatrix}$	$\begin{bmatrix} \cdot & d & \cdot \\ d & \cdot & \cdot \\ \cdot & \cdot & \cdot \end{bmatrix}$	$\begin{bmatrix} \cdot & \cdot & e \\ \cdot & \cdot & \cdot \\ e & \cdot & \cdot \end{bmatrix}$	$\begin{bmatrix} \cdot & \cdot & \cdot \\ \cdot & \cdot & -e \\ \cdot & -e & \cdot \end{bmatrix}$

Table I. Nonzero elements of the Raman tensor and the irreducible representation labels for each of the Raman-allowed vibrational modes present in the D_{4h} tetragonal point group. The same tensors correspond to A_1, B_1, B_2, E(x) and -E(y) modes in point group C_{4v} (Ref. [22]).

$$S\big((i)\big) = \sum_{n=1}^{l_i} \left| \mathbf{e}_i \cdot \mathbf{R}\big((i),n\big) \cdot \mathbf{e}_s \right|^2 . \qquad (1)$$

$\mathbf{e}_i$ and $\mathbf{e}_s$ are respectively incident and scattered electric field unit vectors, $\mathbf{R}$ is the Raman tensor, (i) labels an irreducible representation, l_i its degeneracy, and n numerates the degenerate partners. Other sources [22] have summed the amplitudes from each partner instead of their intensities. For (112) Cd_3As_2 this substantially changes the selection rules, depending on the sign of the E_g mode Raman tensors found in conflicting references [21,22,23,24]. Our results agree with Eq. 1 and are therefore independent of the sign of the E_g tensors. S is evaluated in Table II for all the polarizations used here. It shows, for example, that the doubly degenerate E_g modes must be absent from all backscattering measurements along $\hat{\boldsymbol{z}}$ whereas they are allowed along $\boldsymbol{g}$.

3. Results and discussion

3.1 Cd_3As_2

(001)				
Pol. / Mode	$\bar{z}(XX)z$	$\bar{z}(\acute{X}\acute{Y})z$	$\bar{z}(\acute{X}\acute{X})z$	$\bar{z}(XY)z$
A_1	$\lvert a\rvert^2$	0	$\lvert a\rvert^2$	0
B_1	$\lvert c\rvert^2$	$\lvert c\rvert^2$	0	0
B_2	0	0	$\lvert d\rvert^2$	$\lvert d\rvert^2$
E	0	0	0	0
(112)				
Pol. / Mode	$\bar{g}(AC)g$		$\bar{g}(AA)g$	$\bar{g}(CC)g$
A_1	0		$\lvert a\rvert^2$	$\lvert a+2b\rvert^2/9$
B_1	$\lvert c\rvert^2/3$		0	0
B_2	0		$\lvert d\rvert^2$	$\lvert d\rvert^2/9$
E	$2\lvert e\rvert^2/3$		0	$8\lvert e\rvert^2/9$
(112) twinned				
Pol. / Mode	$\bar{g}(AC)g$		$\bar{g}(AA)g$	$\bar{g}(CC)g$
A_1	$\lvert a-b\rvert^2/18$		$\frac{3\lvert a\rvert^2+a^*b+b^*a+\lvert b\rvert^2}{6}$	$\frac{3\lvert a\rvert^2+a^*b+b^*a+\lvert b\rvert^2}{6}$
B_1	$\lvert c\rvert^2/6$		$\lvert c\rvert^2/6$	$\lvert c\rvert^2/6$
B_2	$2\lvert d\rvert^2/9$		$\lvert d\rvert^2/3$	$\lvert d\rvert^2/3$
E	$4\lvert e\rvert^2/9$		$2\lvert e\rvert^2/3$	$2\lvert e\rvert^2/3$

Table II. Raman scattering efficiencies *S* calculated from Eq. 1 for the polarizations used in the three growth orientations. Notation of the phonon modes are generalized to include all the tetragonal point groups. The polarizations are described in the Porto notation with vectors defined in the text. Colors in these labels are consistent with plot line colors in Figs. 1-3. Constants *a*, *b*, *c*, *d*, and *e* are independent Raman tensor elements defined in Table I. Equally weighted averaging is used for the twinned growth. The twinned growth results hold for any parallel or orthogonal polarization pair in the (112) growth plane.

Figure 1 shows the measured spectra using the polarizations in Table I for a (001) and a (112) sample. Vertical markers identify Raman frequencies and are identical for both orientations. The large number of lines are labeled with an arbitrary number for reference. Effective polarization purity has been attained, as verified by the (001) data of Figure 1(a). Strong

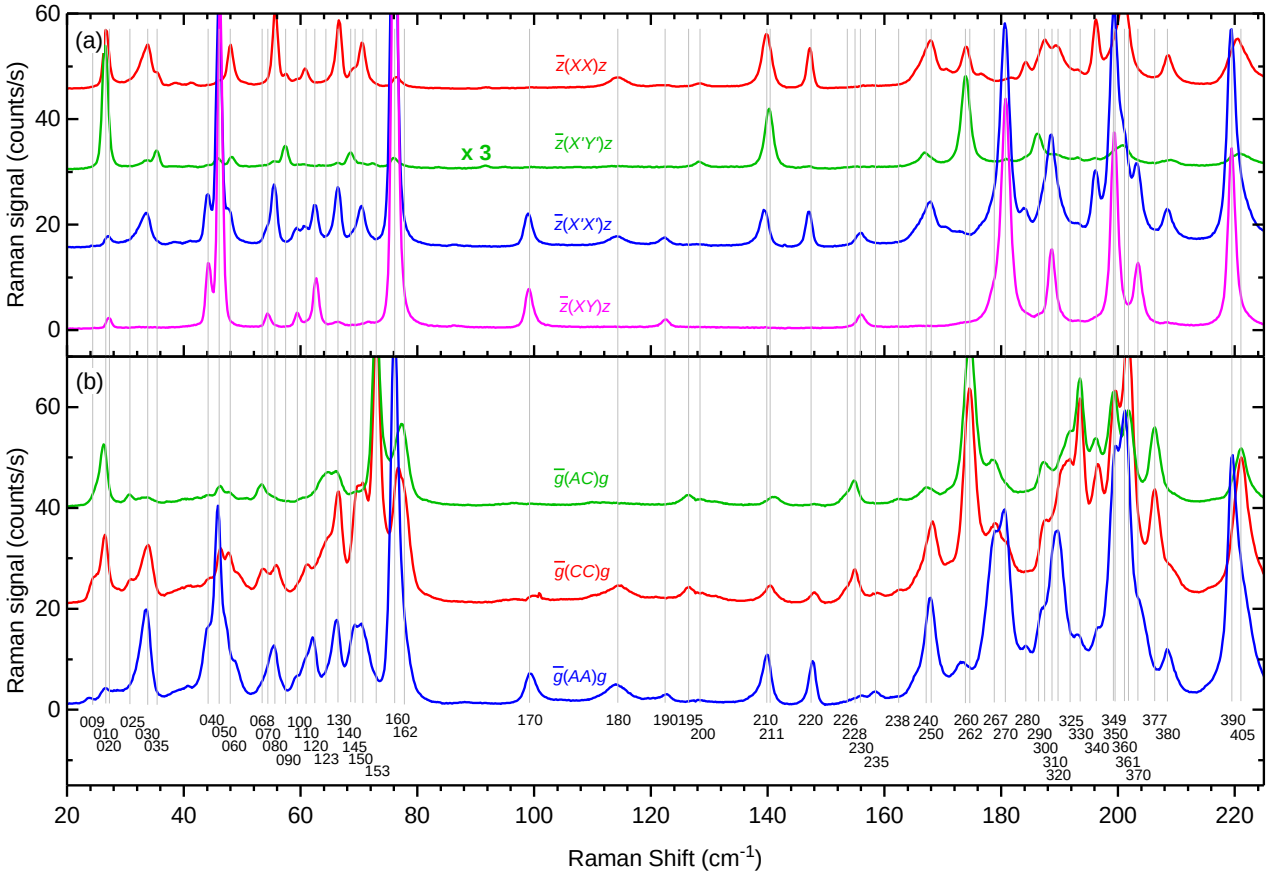

Figure 1. Raman spectra measured using the polarizations shown and (a) (001) backscattering and (b) (112) backscattering. Vertical lines indicate frequencies of Raman modes selected for analysis and numbers are arbitrary reference labels corresponding to entries to Table III.

contrast is seen at frequencies such as lines 210 and 220, where the intensity in the $\bar{z}(XY)z$ curve is 1-2 order of magnitude below that in $\bar{z}(\acute{X}\acute{X})z$. For the (112) grown sample used in Fig. 1(b) this is also true as seen, e.g., in the strong contrast of the $\bar{g}(CC)g$ and $\bar{g}(AA)g$ results of line 153, identified as an E mode. Under different growth conditions however, very different polarization properties were found in Fig. 2(a) where the two parallel-polarized combinations are identical, yet distinct from the cross-polarized signal. This was found in epilayers grown on on-axis substrates, though not exclusively. Figure 2(b) shows that the same sample exhibits a

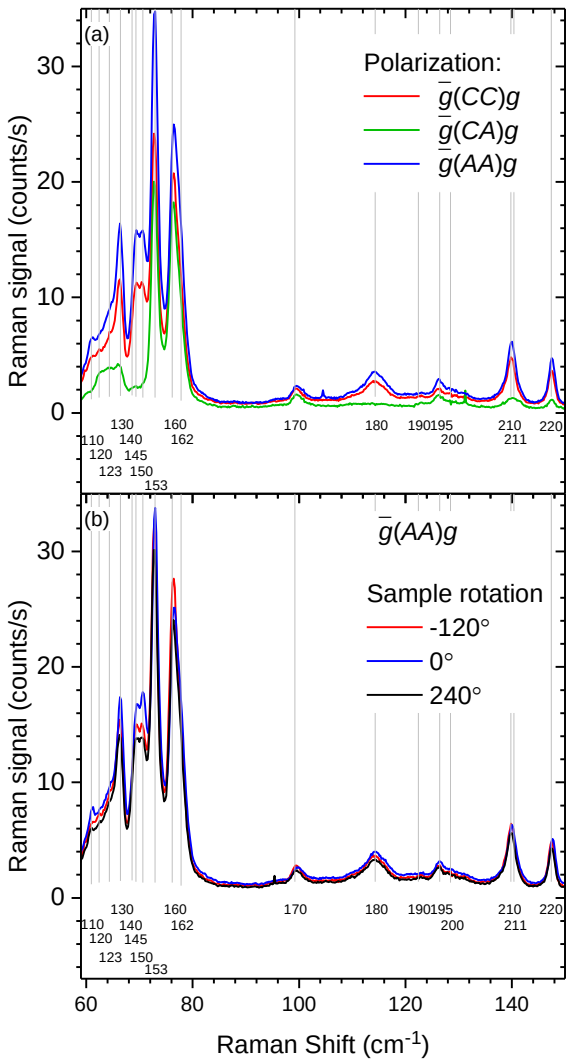

Figure 2. Raman signal in the center frequency region of the twinned (112) growth. In (a) the same polarization combinations of Fig. 1(b) exhibit reduced polarization contrast, and in (b) the results are invariant under 120° rotations of the sample. Similar invariance was seen in $\bar{g}(CC)g$ and $\bar{g}(CA)g$.

three-fold rotation symmetry. This apparent C_3 equivalence is incompatible with the Raman tensor and a single sample orientation. However, it can be understood from a twinning that forms as the Cd_3As_2 grows on the zincblende (111) substrate. There are three primary variants that may each occur with its anion sublattice nearly continuous with the substrate. In these the Cd_3As_2 *c*-axis is aligned along the substrate's [001], [010], or [001] directions. In addition, three secondary variants rotated an angle of π from the primaries may occur when the anion sublattice reverses its stacking sequence at the interface. XRD results show that the vicinal substrates suppress secondary variants, but it is insensitive to the possibility of primary twinning. Conversely, normal-incidence Raman scattering does not distinguish between a primary variant and its corresponding secondary. We therefore hypothesize a three-fold primary twinning is present without addressing whether any secondary variants are also present. The scattered light intensity from a spatial domain consisting of a single variant is modified from Eq. 1 to

$$S\left(\left(i\right)\right)=\sum_{n=1}^{l_i}\left|\mathbf{e}_{\mathrm{i}}\cdot\mathbf{O}^{-1}\cdot\mathbf{R}\left(\left(i\right),n\right)\cdot\mathbf{O}\cdot\mathbf{e}_{\mathrm{s}}\right|^{2} \quad (2)$$

where **O** is a rotation matrix for a -2π/3, 0, or 2π/3 rotation about the substrate's [111] axis. Similar 4-fold twinning in microscopic domains of epitaxial GaAs was modelled by averaging contributions like Eq. (2) from each domain type [25]. The average scattered intensity for an equal distribution of the three Cd_3As_2 variants is given in Table I where it is seen that for parallel analyzed scattering, and for any Raman mode, the signal is identical for light polarized along *A* or *C* in agreement with Fig. 2(a). These twinned selection rules in Table II provide an additional tool for identifying Cd_3As_2 modes through the intensity ratio of the cross-polarized and polarized Raman signals. For the twinned A_{1g} modes this ratio could be small or large depending on the magnitudes and relative argument of the two complex Raman tensor elements, *a* and *b*. Similar measurements have been used to quantify these values in a tetragonal crystal [26]; here we simply note that Table II requires all modes other than A_{1g} to have intensity ratios close to unity in twinned samples. Ratios that are observed in Fig. 2(a) to be much less than unity such as lines 150 and 210 are therefore identified as A_{1g}. In concert with the other selection rules, this allows the peaks in Fig. 1 to be assigned the irreducible representations shown in Table III.

Label	Mode	Frequency (cm^{-1})	Match quality	Ref. [12]	Label	Mode	Frequency (cm^{-1})	Match quality	Ref. [12]
009	E_g	24.4	2		211	B_{1g}	140.2	2	
010	B_{1g}	26.6	1	27.4, B_{1g}	220	A_{1g}	147.5	3	147.4, A_{1g}
020	B_{2g}	27.2	1		226	E_g	153.6	3	
025	E_g	30.7	2		228	E_g	154.9	3	155.0, B_{2g}
030	A_{1g}	33.8	3		230	B_{2g}	155.9	2	
035	B_{1g}	35.4	1		235		158.4	1	
040	B_{2g}	44.2	3		238	E_g	162.4	2	
050	B_{2g}	46.0	3	46.7, E_g	240	B_{1g}	167.1	2	
060	A_{1g}	48.0	2	48.3, B_{2g}	250	A_{1g}	168.0	3	
068	E_g	53.4	3		260	B_{1g}	173.9	2	174.7, B_{1g}
070	B_{2g}	54.4	1		262	E_g	174.6	3	
080	A_{1g}	55.5	3	56.0, B_{1g}	267	B_{2g}	178.8	2	
090	B_{1g}	57.4	2		270	B_{2g}	180.7	3	181.4, B_{2g}
100	B_{2g}	59.4	2		280	A_{1g}	184.2	2	
110	A_{1g}	60.9	2		290	B_{1g}	186.4	1	
120	B_{2g}	62.4	2		300	A_{1g}	187.4	1	187.5, B_{1g}
123	E_g	64.3	2		310	B_{2g}	188.7	1	
130	A_{1g}	66.4	3	66.8, B_{1g}	320	A_{1g}	189.7	2	
140	B_{1g}	68.6	1		325	E_g	191.8	1	
145	A_{1g}	69.3	2		330	E_g	193.5	3	193.6, B_{1g}
150	A_{1g}	70.7	3		340	A_{1g}	196.5	2	196.4, B_{1g}
153	E_g	72.9	3	72.8, B_{1g}	349	E_g	199.2	1	
160	B_{2g}	76.4	3	76.3, E_g	350	B_{2g}	199.5	2	199.2, B_{1g}
162	E_g	77.7	3	77.6, E_g	360		201.1	1	201.0, B_{1g}
170	B_{2g}	99.0	3		361	E_g	201.8	2	
180	A_{1g}	114.3	3	114.2, A_{1g}	370	B_{2g}	203.4	2	
190	B_{2g}	122.5	2	121.7, A_{1g}	377	E_g	206.3	3	206.3, B_{1g}
195	E_g	126.4	3	126.8, B_{2g}	380	A_{1g}	208.5	3	
200	B_{1g}	128.4	1		390	B_{2g}	219.5	3	
210	A_{1g}	139.8	3	140.0, A_{1g}	405		221	1	

Table III. Identification and frequencies of the Raman lines with the label numbers shown in Figure 1. Match quality is a count of each line's consistency with the three sets of selections rules: (001), (112), and (112) twinned.

Along with the label numbers and frequencies, the 4th column of Table III gives a semi-quantitative assessment of the consistency in this identification. This quantity is the number (1-3) of selection rule sets that are in agreement for the identification. For example, line 170 is present in both $\bar{z}(XY)z$ and $\bar{z}(\acute{X}\acute{X})z$ of Fig. 1(a), indicating B_{2g}. This is confirmed by strong and weak signals in $\bar{g}(AA)g$ and $\bar{g}(CC)g$ respectively in Fig. 1(b) and confirmed a third time by strong cross-polarized signal for the twinned sample. Some lines were not confirmed across all three criteria, usually due to weak signal or their inability to be distinguished from neighbors in crowded spectral regions. A small number were given no assignment due to conflicting

polarization behavior. The last column in Table III lists the frequency and identification given for the same line in Ref. [12]. Entries into this column were only made for lines that are relatively strong or isolated, allowing unambiguous correspondence with the measurements of Ref. [12]. The total mode count from Table III is 16 A_{1g} + 9 B_{1g} + 16 B_{2g} + 16 E_g plus three unassigned lines, slightly exceeding some of the individual counts predicted for $I4_1/acd$. This violation is likely just a reflection of the uncertainty noted in Table III rather than evidence for a lower-symmetry space group.

The former [4] Cd_3As_2 group assignment, $I4_1cd$, belongs to a piezoelectric crystal class and it would be predicted to exhibit, in addition to the much larger mode count noted above, a longitudinal-transverse splitting due to the separate Raman contributions from the deformation potential and electric field [27]. This would further increase the number of Raman frequencies predicted for (112) growth far beyond what is observed here. A further test is the comparison of $\bar{z}(\acute{X}\acute{X})z$ and $\bar{g}(AA)g$ spectra in Fig. 1. They contain equivalent light polarization directions, differing only in their phonon displacement directions and thus should be identical in the absence of longitudinal-transverse splitting. Fig. 1 shows that while there is some difference in relative signal strength, notably at lines 267 and 340, the spectra are otherwise in agreement, thus confirming a non-piezoelectric crystal class.

3.2 $(Cd_{1-x}Zn_x)_3As_2$

The effect of Zn incorporation is studied in Fig. 3 which shows polarized spectra for (112) samples of $(Cd_{1-x}Zn_x)_3As_2$ with increasing amounts of Zn. The Zn/As flux ratio during growth was recorded as a proxy for the composition fraction, *x*. At higher flux ratios *x* could be verified from XRD, confirming that Zn pressure undercounts the composition fraction, but is still a good estimate for the concentrations used here, on the order of a few percent. With increasing Zn composition, the spectra in Fig. 3 are rapidly broadened, with nearby lines often merging together. In addition, the loss of polarization contrast first seen in Fig. 2 occurs here. Contrast

decreases such that the two parallelly-polarized spectra become very similar, yet still distinct from the $\bar{g}(CA)g$ orthogonal spectrum. This can be understood from twinning that is restrained by the intentional substrate misorientation in the case of Cd_3As_2, but rapidly appears with increasing Zn concentration. XRD data is consistent with, but not unique to this hypothesis.

Another possible explanation for a Raman polarization transition in Cd_3As_2 involves the intermediate and high temperature phases that form due to thermally activated disordering of the Cd vacancies, first into a smaller tetragonal unit cell and finally into a fully disordered cubic phase, respectively [2]. The intermediate $P4_2/nmc$ α'' phase has been found to be room temperature stable under addition of zinc and occasionally in pure Cd_3As_2 [9]. The data of Fig. 1 could then be interpreted as the fully ordered $I4_1/acd$ phase upon which the addition of Zn in Fig. 3 disrupts the ordering and restores a higher symmetry phase. However, neither the α'' nor the high temperature β phase are candidates for the data of Fig. 3 where Zn addition is seen to relax the

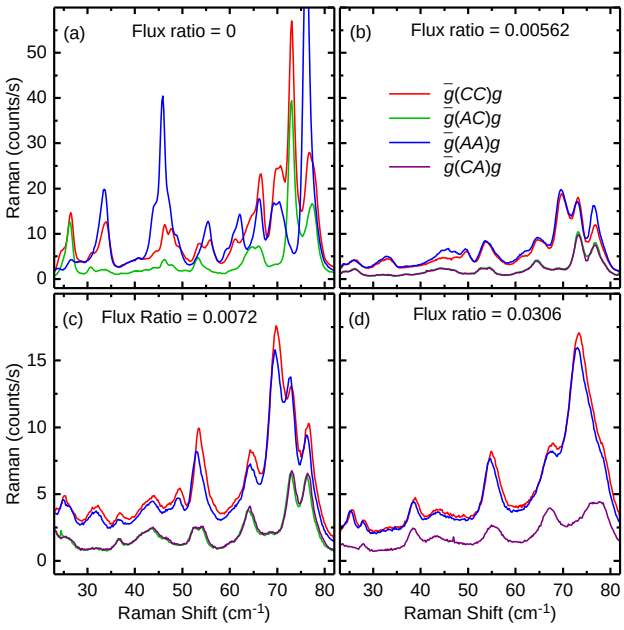

Figure 3. (a) – (d), the low-frequency Raman spectra of (112) $(Cd_{1-x}Zn_x)_3As_2$ for four different Zn composition fractions, *x*. The polarization legend applies to each panel and redundant cross polarizations are shown for (b) and (c).

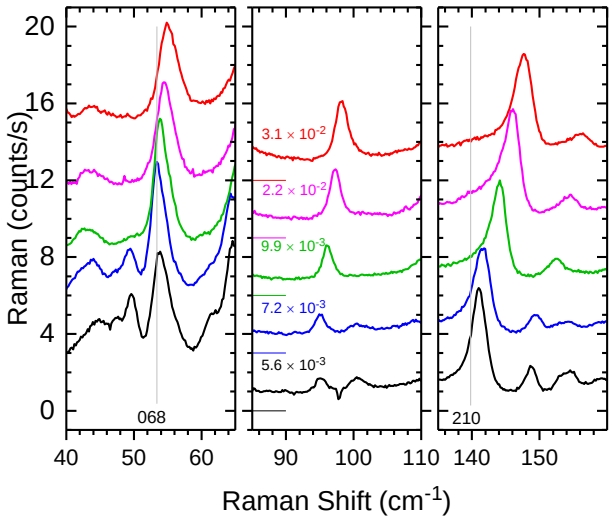

Figure 4. Concentration dependence of three $(Cd_{1-x}Zn_x)_3As_2$ lines in the $\bar{g}(CC)g$ polarization, measured in 5 samples grown with the Zn/As flux ratios shown. Curves are vertically offset by the baselines shown in the center panel.

polarization selection rules while keeping a relatively dense Raman spectrum. β-Cd_3As_2 has the CaF_2 structure with only one Raman active mode. For α''-Cd_3As_2, the site symmetries given in Ref. [9] are three sets of Cd 8(*g*), 1 As 8(*f*), 1 As 4(*d*), and 1 As 4(*c*). This yields 9 A_{1g} + 10 B_{1g} + 4 B_{2g} + 16 E_g Raman active modes but they would still have the tetragonal selection rules. Neither phase explains Figs. 1-3 and we therefore retain the interpretation of rotated α-Cd_3As_2 domains.

The addition of Zn also modifies the Raman frequencies. The progression is difficult to follow for many lines, due to an abrupt change at the lowest nonzero concentration, or due to strong broadening. However, three exceptions are plotted in Fig. 4. The general effect is an increase in frequency with Zn concentration and this varies from a weak dependence for line 068, to a much stronger dependence in line 210. The shift of the latter, changing by 7 cm^{-1}, is larger than that found in e.g., $Al_xGa_{1-x}As$ where phonon shifts are $\leq$ 0.7 cm^{-1} per % Al [28]. Line 210 also shifts more than what would be expected from epitaxial strain due to a few percent of Zn. As noted above, the Cd_3As_2 epilayer is lattice matched to its $Zn_{1-x}Cd_xTe$ buffer. Its lattice mismatch with pure Zn_3As_2 is 7.5% [2,16] and strain-induced Raman shifts in other materials are 4 cm^{-1} per % strain in GaAs [29] and 7 cm^{-1} per % strain in Si [30]. Regardless of their size, the shifts of lines 068 and 210 could be understood as a one-mode phonon behavior in which the phonon frequency of the quasi-crystal alloy is a linear interpolation of its endpoints due to the averaging of cation mass and bonding strength. Broadening from alloy fluctuations, and orientational averaging due to twinning would also be present. Opposing this simple interpretation, however, is a more significant change seen in the line beginning at 95 cm^{-1} which was not detected in pure Cd_3As_2 but appears with increasing strength and frequency as the Zn content is increased. Being absent in every polarization of Fig. 1, it cannot be explained by relaxed selection rules due to disorder. Its behavior is that of a two-mode alloy in which a Zn-like phonon has a strength proportional to the Zn concentration and a frequency beginning at a Zn local mode in Cd_3As_2, i.e., 95 cm^{-1}. Continuity with Zn_3As_2 could not be verified due to broadening within the very dense spectra. The clean two-mode behavior was only observed at 95 cm^{-1}, possibly because this spectral region is fortuitously isolated from other phonons. One- and two-mode phonons are sometimes observed together in complicated crystals.

For the one-and two-mode labels to be applicable across the full composition range, the alloy should be composed of isomorphic endpoints, which is not the present understanding of Cd_3As_2 and Zn_3As_2. An alternative explanation of Fig. 4 is that the low-Zn alloy undergoes an abrupt transition to the $I4_1cd$ structure and gains new Raman-active phonons allowed by the noncentrosymmetric group. This explanation, however, relies on the two space group assignments, which are not equally certain. The α phase of Zn_3As_2 was first proposed [31] to be $I4_1/acd$ until a later study of the phase transitions found instead $I4_1cd$ [16]. However the techniques of that study, which also included Cd_3As_2, were not able to distinguish a difference in the α phase space groups of the two compounds. They were long accepted as isomorphic until Cd_3As_2 and particularly its centrosymmetry became the subject of a recent study [2]. A similar measurement of Zn_3As_2 may be required for full understanding of the alloy $(Cd_{1-x}Zn_x)_3As_2$ and the results of Fig. 4. This has potentially far-reaching consequences for Cd_3As_2 research since Zn alloying allows manipulation of the DSM phase [10] as well as control over the Fermi level through compensation of the intrinsic n-doping from As vacancies in Cd_3As_2.

Acknowledgments

We thank Phil Parilla for useful discussions. This work was authored by the National Renewable Energy Laboratory, operated by Alliance for Sustainable Energy, LLC, for the U.S. Department of Energy (DOE) under Contract No. DE-AC36-08GO28308. Funding provided by the U.S. Department of Energy, Basic Energy Sciences. The views expressed in the article do not necessarily represent the views of the DOE or the U.S. Government.

References

[1] I. Crassee, R. Sankar, W.-L. Lee, A. Akrap, and M. Orlita, Phys. Rev. Mater. **2**, 120302 (2018).
[2] M. N. Ali, Q. Gibson, S. Jeon, B. B. Zhou, A. Yazdani, and R. J. Cava, Inorg. Chem. **53**, 4062 (2014).
[3] H. Kim, M. Goyal, S. Salmani-Rezaie, T. Schumann, T. N. Pardue, J.-M. Zuo, and S. Stemmer, Phys. Rev. Mater. **3**, 084202 (2019).
[4] G. A. Steigmann and J. Goodyear, Acta Crystallogr. Sect. B **24**, 1062 (1968).
[5] S. Wei, J. Lu, W. Yu, H. Zhang and Y. Qian, Cryst. Growth Des. **6**, 849 (2006).
[6] K. Zhang, H. Pan, M. Zhang, Z. Wei, M. Gao, F. Song, X. Wang, and R. Zhang, RSC Adv. **7**, 17689 (2017).
[7] G. Pangilinan, R. Sooryakumar, B. Chelluri, and T. Y. Chang, Phys. Rev. Lett. **62**, 551 (1989).
[8] E. Z. Stutz, M. Friedl, T. Burgess, H. H. Tan, P. Caroff, C. Jagadish and A. Fontcuberta i Morral, Phys. Stat. Sol. RRL, 1900084 (2019).
[9] A. Pietraszko and K. Lukaszewicz, Acta. Cryst. B**25**, 988 (1969).

[10] S. Nishihaya, M. Uchida, Y. Nakazawa, R. Kurihara, K. Akiba, M. Kriener, A. Miyake, Y. Taguchi, M. Tokunaga, and M. Kawasaki, Nat. Commum. **10**, 2564 (2019).
[11] T. Schumann, L. Galletti, D. A. Kealhofer, H. Kim, M. Goyal, and S. Stemmer, Phys. Rev. Lett. **120**, 016801 (2018).
[12] A. Sharafeev, V. Gnezdilov, R. Sankar, F. C. Chou, and P. Lemmens, Phys. Rev. B **95**, 235148 (2017).
[13] J. Weszka, M. Renucci, and A. Zwick, phys. stat. sol. (b) **133**, 57 (1986).
[14] W. G. Fateley, N. T. McDevitt and F. F. Bentley, Appl. Spectro. **25**, 155 (1971).
[15] J. Misiewicz, Infrared Phys. Technol. **35**, 781 (1994).
[16] A. Peitraszko and K. Lukaszewicz, phys. stat. sol. (a) **18**, 723 (1973).
[17] ICSD (2007). Inorganic Crystal Structure Database. FIZ-Karlsruhe, Germany,and the National Institute of Standards and Technology (NIST), USA. http://www.fiz-karlsruhe.de/icsd.html
[18] A. D. Rice, K. Park, E. T. Hughes, K. Mukherjee, K. Alberi. Phys. Rev. Mat. **3**, 121201(R) (2019).
[19] T. Schumann, M. Goyal, H. Kim, S. Stemmer, APL Mater. **4**, 126110 (2016).
[20] M. Goyal, L. Galletti, S. Salmani-Rezaie, T. Schumann, D. E. Kealhofer, and S. Stemmer, APL Mater. **6**, 026105 (2018).
[21] H. Poulet, J. P. Mathieu, Vibration Spectra and Symmetry of Crystals, Ch.9 (Gordon and Breach, 1976).
[22] D. F. Edwards, Raman Scattering in Crystals, UCID-21510, Lawrence Livermore National Laboratory, Livermore, California (1988), pp. 19-22.
[23] W. Hayes, R. Loudon: *Scattering of Light by Crystals* (Wiley, New York 1978).
[24] M. I. Aroyo, A. Kirov, C. Capillas, J. M. Perez-Mato & H. Wondratschek "Bilbao Crystallographic Server II: Representations of crystallographic point groups and space groups" Acta Cryst. **A62**, 115-128 (2006).
[25] G. Landa, R. Carles, J. B. Renucci, C. Fontaine, E. Bedel, and A. Muñoz-Yague, J. Appl. Phys. **60**, 1025 (1986).
[26] T. Strach, J. Brunen, B. Lederle, J. Zegenhagen and M. Cardona, Phys. Rev. B **57**, 1292 (1998).
[27] I. Gregora, *International Tables for Crystallography, Vol. D*, Ed. A. Authier, Ch. 2.3, pp. 314-328 (2006).
[28] M. Ilegems and G. L. Pearson, Phys. Rev. B **1**, 1576 (1970).
[29] H. Shen and F. H. Pollak, Appl. Phys. Lett. **45**, 692 (1984).
[30] J. Munguia, J.-M. Bluet, H. Chouaib, G. Bremond, M. Mermoux, and C. Bru-Chevallier, J. Phys. D: Appl. Phys. **43** 255401 (2010).
[31] H. Cole, F. W. Chambers and H. M. Dunn, Acta Cryst. **9**, 685 (1956).